Towards on-chip mid-infrared sensors

Journal:	*Analytical Chemistry*
Manuscript ID	ac-2015-04143f.R1
Manuscript Type:	Feature
Date Submitted by the Author:	n/a
Complete List of Authors:	Sieger, Markus; University of Ulm, Institute of Analytical and Bioanalytical Chemistry Mizaikoff, Boris; Ulm University, Institute of Analytical and Bioanalytical Chemistry

Towards on-chip mid-infrared sensors

Markus Sieger and Boris Mizaikoff*

Institute of Analytical and Bioanalytical Chemistry, Ulm University, Albert-Einstein-Allee 11, 89081 Ulm, Germany

thin-film waveguide, on-chip, photonics, mid-infrared (MIR), infrared spectroscopy, infrared sensors, chem/bio sensors, quantum cascade laser (QCL), interband cascade laser (ICL), label-free

ABSTRACT: This feature highlights recent advances on mid-infrared thin-film waveguide technology and on-chip photonics facilitating next-generation label-free chem/bio sensor and assay platforms. Complemented by more recent advancements towards on-chip semiconductor waveguides it is anticipated that label-free integrated mid-infrared sensing schemes will readily complement existing chem/bio sensor technologies in applications ranging from process monitoring and environmental analysis to biomedical diagnostics and point-of-care devices.

INTRODUCTION

Mid-infrared (MIR, 2.5-20 μm) spectroscopy provides highly discriminatory information on organic and inorganic molecules due to the excitation of vibrational and rotational transitions that are specific to these species in liquid, gas, and solid phase. Hence, the MIR spectral regime is particularly attractive for establishing optical chem/bio sensor technologies taking advantage of this inherent molecular selectivity.[1] However, despite the versatility and discriminatory power of the MIR electromagnetic window, most spectroscopic and sensing applications remain confined to a laboratory environment, in part due to the dimensions of conventional IR spectroscopic equipment.[2] Yet, considering the already achieved miniaturization and on-chip integration for optical sensors operating in the ultraviolet-to-visible (UV-Vis) and near-infrared (NIR) regime, the application opportunities for integrated and potentially even on-chip MIR sensing platforms are immediately evident, as in-situ chem/bio sensing via vibrational molecular signatures is enabled.[3] MIR sensing system generally comprise three major components: (i) the MIR light source, (ii) appropriate waveguide structures propagating the IR radiation and frequently also serving as the active optical transducer (a.k.a., sensor head), and (iii) the MIR detector. Among the available radiation sources, quantum cascade lasers (QCL) and interband cascade lasers (ICLs) are nowadays unambiguously accepted as the most advanced light source technology for realizing compact MIR sensing devices.[4–7]In contrast to conventional semiconductor lasers, QCLs and ICLs are based on quantum heterostructures modulating the thickness of the quantum well rather than the composition of the active medium for tailoring the light emission wavelength occurring via intersubband and interband transitions, respectively. Last but not least, such lasing structures provide exceedingly compact dimensions, high optical output power, long lifetimes and operational stability, availability across almost the entire MIR spectral range, and broad wavelength tunability up to >250 cm^{-1} for a single external cavity-coupled device.[8,9] In particular, the utility of QCLs as an advanced light source for highly sensitive waveguide-based evanescent field absorption sensing concepts has recently been demonstrated.[10–12] While most MIR sensor applications still use either thermoelectrically or liquid-nitrogen cooled semiconductor detectors (e.g., made from mercury-cadmium-telluride, indium-antimonide or similar mixed semiconductors), quantum heterostructures similar to QCL technology have shown promising results serving as quantum cascade detectors (QCDs), which facilitates further miniaturization and on-chip integration.[13] Last but not least, advancements on the miniaturization and enhancement of the sensitivity for pyroelectric and thermopile detectors has lead to inexpensive MIR detectors at highly compact dimensions.[14–18] However, on-chip integration of MIR sensors remains a veritable challenge, as the third crucial component for establishing functional MIR sensing platforms rests in its infancy: thin-film MIR waveguides matched in their light propagation properties to the coherent radiation provided by QCLs and ICLs. MIR waveguides useful for sensing applications (i.e., optical fibers and planar waveguide structures) are usually fabricated from a very limited set of IR-transparent materials dominated by polycrystalline silver halides[19,20], tellurium halides[21,22], and amorphous chalcogenide glasses[23] usually fabricated with waveguide dimensions (i.e., thicknesses) limited to the range of several tens to several hundreds of micrometers.

Consequently, this feature article focuses on recently emerging thin-film waveguide technologies suitable for the MIR spectral window, which pave the way towards the anticipated on-chip integration of entire MIR chem/bio sensing systems or assays, and subsequently, towards IR-lab-on-a-chip platforms.

WHY THIN-FILM WAVEGUIDES?

Attenuated total reflection (ATR) spectroscopy (a.k.a., evanescent field absorption spectroscopy) in the MIR spectral regime is nowadays routinely used for the analysis of thin films, liquids, and solids taking advantage of the generic concept of total internal reflection (TIR). TIR occurs, if light is

reflected at an incident angle exceeding the so-called critical angle with $\theta_c = \sin^{-1}(n_c/n_{wg})$ at the interface between a waveguide and an adjacent medium (1), and if the refractive index (RI) of the waveguide (n_{wg}) is larger than that of the surrounding material (n_c). Part of the electromagnetic field (a.k.a., evanescent field, evanescent wave or leaky mode) then leaks into the adjacent environment with an exponentially decaying field intensity at increasing distance for the waveguide surface. The penetration depth of the evanescent field (d_p) at a certain wavelength λ may be approximated via[20]

$$d_p = \frac{\lambda}{2\pi\sqrt{n_{wg}^2 \sin^2\theta - n_c^2}}$$

A more detailed discussion of the evanescent field goes beyond the scope of this feature; the interested reader is therefore referred to the pertinent literature[24,25]. If analyte molecules are present at the waveguide surface or within d_p, they may interact with the evanescent field generated at the waveguide-sample interface, which in case of light absorption leads to the attenuation of the propagating wave at the frequencies in resonance with corresponding molecular vibrations and/or rotations. Thereby, an IR-ATR absorption spectrum is generated.[1] The absorption within the evanescent field follows a pseudo Beer-Lambert relationship, thus enabling quantification of the obtained molecular signatures following

$$A = (ecl)r = \log(\frac{I_0}{I})$$

with I_0 as the initial light intensity, I as the intensity after analyte interaction, ε as the molar absorptivity, c the concentration, and r as the fraction of radiative energy residing outside the waveguide (i.e., within the evanescent field).[10,24–26] Consequently, increasing the intensity of the evanescent field directly affects the obtainable signal-to-noise ratio (SNR) during an absorption measurement, and therefore directly enhances the sensitivity of the corresponding measurement. In turn, the intensity of the evanescent field depends on the dielectric constant at the waveguide-sample interface, which is itself dependent on the involved materials, and the cross-sectional dimensions and thickness of the waveguide. In conclusion, for maximizing the SNR during evanescent field absorption measurements it is essential tailoring the waveguide thickness, structure, and geometry as the key parameters for directly enhancing the achievable analytical sensitivity.

However, the thickness of most conventionally applied MIR waveguides is significantly larger than the wavelength of the propagating radiation. Total internal reflection (i.e., as a reflection following conventional ray optics) therefore occurs only a few times along the long axis of the waveguide, and consequently results in a rather limited effective interaction path length. Correspondingly, the achievable sensitivity is limited. Since the number of reflections is inversely proportional to the thickness of the waveguides, decreasing the thickness of the waveguiding layer directly impacts the analytical figures-of-merit.[27] However, once the waveguide thickness reaches the order of magnitude of the wavelength, conventional ray optics resulting in discrete reflections cannot describe the actual propagation behavior of guided waves anymore, as discrete internal reflections overlap and become indistinguishable.[28]

Therefore, simplifying the scenario inside a macroscopic waveguide (i.e., vs. the wavelength of the propagating radiation with $d_{wg}>>\lambda$) ray optics provide a sufficiently accurate description of the beam path within the waveguide structure, as schematically illustrated as a zigzag pattern in Fig. 1a and b. With decreasing waveguide thickness these discrete reflections convolute into a continuous evanescent field generated along the waveguide surface rather then discrete areas responsible for generating the analytical signal (Fig. 1c).

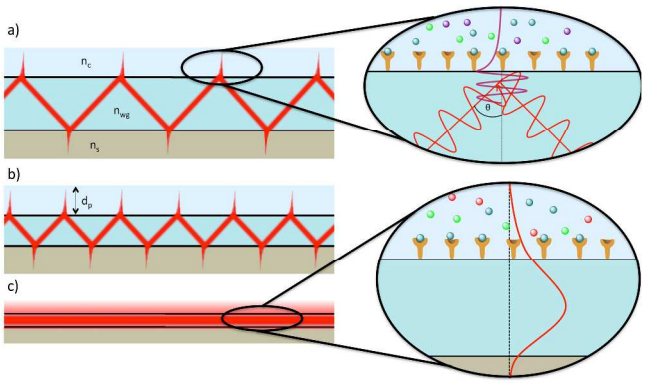

Figure 1. Schematic of a planar waveguide composed of a layer of sample (e.g., analyte-containing solution, solid, etc.) (n_c), a waveguiding layer (n_{wg}), and a substrate layer (n_s) (i.e., in case of a thin-film substrate-supported waveguide structure) with $n_{wg}>n_s,n_c$. (a) The guided radiation propagates via total internal reflections along a zigzag path through the waveguide. (b) As the thickness of the waveguide decreases, the number of internal reflection increases. (c) If the thickness is on the order of magnitude of the wavelength, individual reflections no longer adequately describe the propagation behavior of the wavefront; the evanescent field appears continuously along the entire waveguide surface. Reproduced with permission from ref. 27. Copyright 2005 American Chemical Society.

The latter type of waveguide structure is also known as an integrated optical waveguide (IOW). In the case of IOWs, conventional ray optical models may provide useful approximations, yet, do not adequately describe the propagation of electromagnetic waves inside the waveguide structure. An exact description of the propagation characteristics within IOW requires a full-wave model solving Maxwell's equations, which allows calculating the electric field amplitude across the waveguide structure.[28,29]

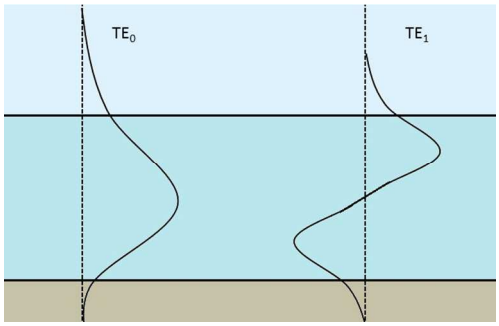

Figure 2. Scheme of waveguide modes within a planar optical waveguide. The field distribution of the fundamental mode (TE_0), and the first order mode (TE_1) are shown.

According to Maxwell's equations, only discrete electromagnetic field distributions satisfy the required boundary conditions, and may thus be guided within a waveguide. The transverse distribution of the first four modes, i.e., the fundamental modes TE_0, TM_0, and the first order modes TE_1, TM_1, respectively are in part schematically illustrated in Fig. 2. Each mode may be viewed as a standing wave traveling in y-direction. The number of guided modes, which may occur within a planar waveguide decreases with decreasing thickness of the waveguiding layer, with and decrease of the refractive index contrast between waveguide and the surrounding medium, and with increasing wavelength. Hence, if for example the thickness of the waveguiding layer is selected to be slightly larger than the accordingly calculated minimum thickness, only fundamental TE_0 and TM_0 modes propagate within the waveguide structure. Such waveguides are correspondingly called *single-mode* waveguides. If the waveguide thickness is further increased, first order modes, second order modes, etc. may be excited, and a so-called *multi-mode* waveguide behavior is evident.

Up to this point, confinement of the propagating wave has only been considered in one direction (i.e., vertical vs. the long axis of the waveguide and propagation direction of the wave, respectively), as defined by the thickness of a planar waveguide (i.e., *slab waveguide*) structure (Fig. 3a). Consequently, propagating radiation may still laterally distribute within the waveguiding layer. Additional (i.e., horizontal) confinement of the radiation significantly increases the fraction of the optical power within the evanescent field.[30] Fig. 3 schematically illustrates the most common waveguide structures enabling single- or multi-mode behavior within a waveguide due to additional lateral confinement vs. conventional slab waveguides (Fig. 3a-d). From a fabrication perspective, several approaches facilitate the generation of such confined waveguiding paths (a.k.a., *channel waveguides*. Usually, a strip of high-RI material is either deposited on top of a substrate with lower RI, or a previously deposited waveguide layer is etched such that a *strip waveguide* is retained (Fig. 3b). If the etching process is stopped before the substrate is reached, a *rib waveguide* has been defined, which is commonly used in the visible regime, as the rib depth and not the entire waveguide thickness defines the modal behavior (Fig. 3c). If a cladding layer is present between substrate and the actual waveguide, a *ridge waveguide* may be defined via appropriate deposition or etching processes (Fig. 3e). By locally increasing the RI of a substrate, an *embedded waveguide* (a.k.a., *buried waveguide*) is created, as shown in Fig. 3f Finally, optical fibers are certainly the most commonly applied types of waveguide with applications especially in telecommunications and for efficiently coupling light into other waveguide-based conduits.[8,31] However, due to the rather limited potential for on-chip integration with the exception of serving as an optical coupling element, a more detailed discussion of fiberoptic waveguide geometries is omitted in this feature; the interested reader is referred to seminal reviews on MIR fiberoptic materials and waveguides.[32–37]

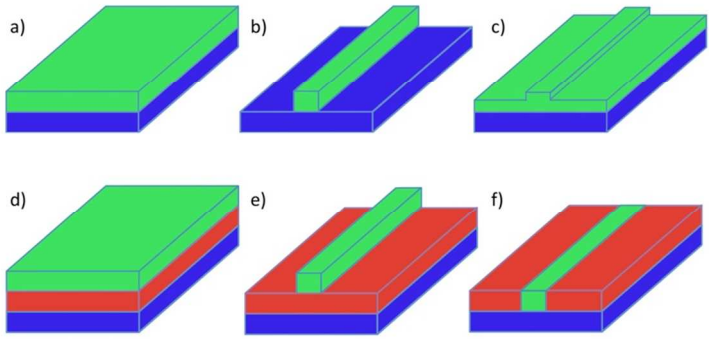

Figure 3. Illustration of common thin-film waveguide geometries. a) slab waveguide, b) strip waveguide, c) rib waveguide with $n_c>n_s$, d) slab waveguide, e) ridge waveguide, and f) embedded/buried waveguide with $n_c>n_b$. The same functional layers are marked with the same colors: green =waveguide layer (n_c), red = optical buffer layer (n_b), blue= substrate (n_s).

Table 1. Selection of MIR transmitting materials applicable for thin-film waveguide fabrication including relevant properties in the MIR spectral regime.

Waveguide material	Transmission range	Refractive index	Selected References
Si	2-6.5 µm	3.426 (@5 µm)	38,39
SiO_2	2-3.5 µm	1.46 (@5 µm)	40,41
Si_3N_4	2-8.5 µm	2.33 (@5 µm)	42,43
AlN	2-10 µm	1.94 (@5 µm)	43,44
Al_2O_3 (Sapphire)	2-6.6 µm	1.52 (@5 µm)	43,45
GaAs	2-16 µm	3.3 (@6 µm)	1,39
Ge	2-14 µm	4.01 (@6 µm)	46,47
As_2S_3	2-6 µm	2.38 (@10.6 µm)	48,49
As_2Se_3	2-9 µm	2.78 (@8.4 µm)	48,49
$Te_2As_3Se_5$	2-12 µm	2.82 (@10.6 µm)	48,50
$Te_{82}Ge_{18}$	6-10 µm	3.44 (@10.6 µm)	49,50
$Te_{75}Ge_{15}Ga_{10}$	6-20 µm	3.40 (@10.6 µm)	49,50

MCT	2-24 µm	4.0 (@5 µm)	51,52
CdTe	2-25 µm	2.68 (@6µm)	39,51
C (Diamond)	2-25 µm	2.38 (@5 µm)	39,40

Among the already limited set of MIR transmitting materials applicable for generating fiberoptic waveguides, there is an even more limited selection of materials for IOW fabrication. The properties of the most relevant thin-film waveguide materials are summarized in Table 1. For comparison with commonly used materials suitable in NIR and VIS sensing applications, the properties of silicon waveguide structures are listed as well. However, the utility of Si in MIR chem/bio sensor technology appears limited to a wavelength of approx. 3.7 µm due to the opacity of SiO_2, which is the most commonly used cladding layer for establishing more sophisticated silicon waveguide structures; the interested reader is therefore referred to the current literature.[53–63]

MID-INFRARED SENSOR TECHNOLOGY BASED ON THIN-FILM WAVEGUIDES

GaAs/AlGaAs Waveguides. Advanced deposition techniques such as metal organic vapor phase epitaxy (MOVPE), physical vapor deposition (PVD), and molecular beam epitaxy (MBE) are nowadays established methods for the fabrication of thin semiconductor layers (e.g., GaAs, AlGaAs, InGaAlP) at well-defined dimensions and compositions. In a collaborative effort, the groups of Mizaikoff and Faist have pioneered the first entirely semiconductor-based thin-film MIR waveguides made from epitaxially grown GaAs/AlGaAs via MBE or MOVPE providing a spectral transmission window of up to 13 µm.[10] Consequently, such semiconductor thin-film waveguides may be considered the fundamental architecture for monolithic or hybridized chip-integrated MIR sensing platforms, and also for more complex MIR photonic structures taking advantage of well-established microfabrication techniques.

The first GaAs/AlGaAs thin-film waveguide structures were grown on a Si-doped GaAs substrate via MBE with a calculated refractive index of n = 2.8. A 6 µm $Al_{0.2}Ga_{0.8}As$ optical buffer layer (n=3.2) was epitaxially deposited followed by the actual waveguiding layer, i.e., a 6 µm GaAs core layer (n=3.3). As shown in Fig. 4, the obtained mode profile is clearly single-mode along the x-axis. A distributed feedback (DFB) QCL was coupled into the waveguide structure providing TM polarized light at a wavelength of 974 cm^{-1}. Radiation emanating at the distal end facet of the slab waveguide was detected via a liquid nitrogen cooled MCT detector. Droplets of acetic anhydride were deposited at the waveguide surface serving as analyte solution ensuring coverage of the evanescent field at the beam waist. According to the coverage length, an absorption signal was calculated based on the observed intensity changes. These pioneering measurements have established the fundamental utility of epitaxially grown semiconductor GaAs/AlGaAs waveguide structures for next-generation MIR waveguide technology in lieu of thus far predominantly applied fiberoptic transducers, thereby facilitating the development of fully integrated on-chip MIR chem/bio sensing devices.

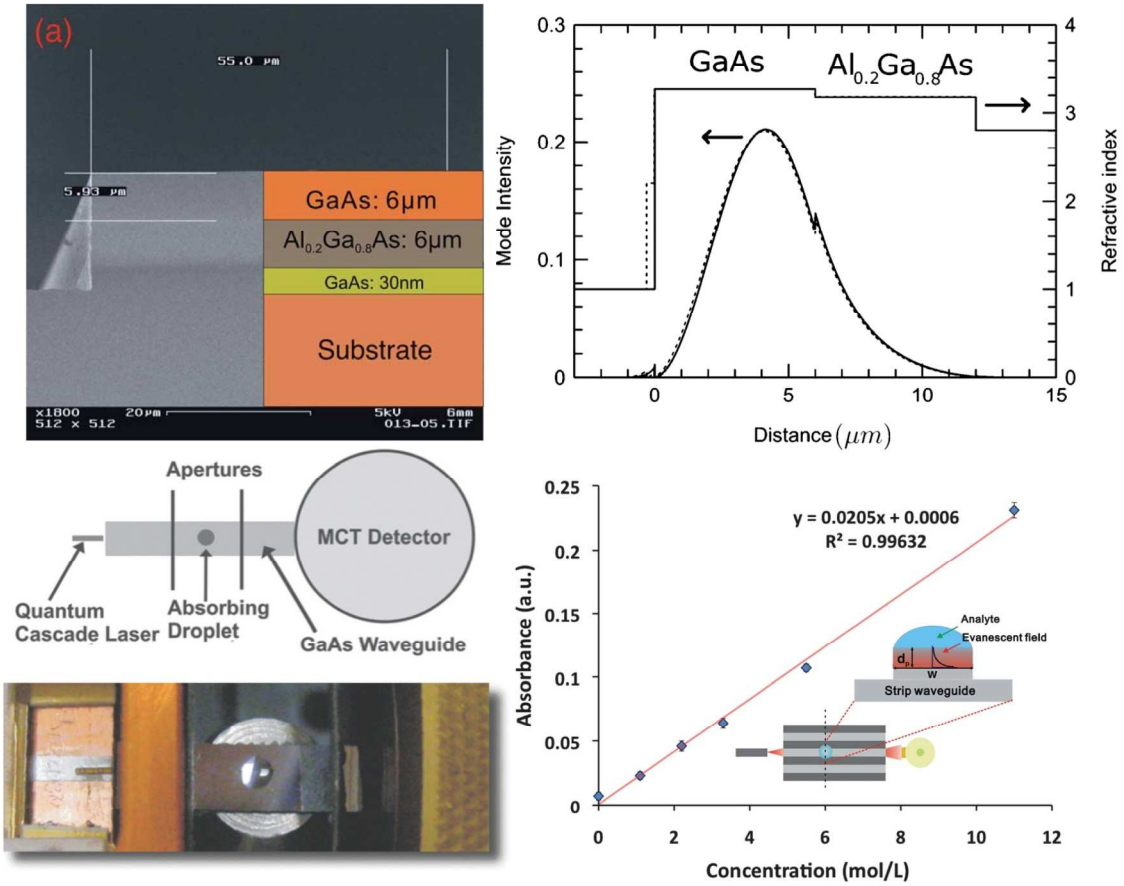

Figure 4. (top left) Cross-section of a MOVPE-grown GaAs/$Al_{0.2}Ga_{0.8}As$ ridge waveguide obtained via reactive ion etching. (top right) Computed optical mode profile of the thin-film GaAs/AlGaAs waveguide structure with layer dimensions of 6 µm (left axis: mode intensity, right axis: refractive index). (bottom left) Experimental setup of a single wavelength emitting QCL pigtail-coupled to a GaAs slab waveguide. (bottom right) Analytical response to 2nL droplets of an analyte in an evanescent field absorption measurement with QCL pigtail-coupled to a structured GaAs ridge waveguide (200 µm in width). Reproduced with permission from ref. 10,30. Copyright 2006 American Chemical Society.

Since such thin-film slab waveguides exclusively promote confinement of MIR radiation perpendicular to the propagation direction, the mode profile changes laterally along the beam propagation path. To ensure lateral confinement, GaAs ridge waveguides at different widths were microfabricated revealing a significant enhancement of the analytical sensitivity during evanescent field absorption experiments.[30] For structuring ridge waveguides, photoresist was spin-coated onto the surface of the wafer and exposed to UV radiation via a manual mask aligner. After the development process, the photoresist waveguide patterns were transferred onto the wafer via reactive ion etching (RIE), i.e., a dry etching process using a mixture of $SiCl_4$ and argon as etching gas. Thereafter, the photoresist was removed and the wafers were cleaved along the crystal axis using a diamond knife for obtaining MIR waveguide chips with dimensions of approx. 5x8 mm. The cleaved facets provided sufficient surface quality for effective coupling of laser radiation. Similar to studies using GaAs slab waveguides, droplets of 2 nL were deposited onto the 200 µm wide ridge waveguide surface via micro-capillaries with tapered tips providing a surface coverage length of approx. 400 µm. After calibration using solutions of the analyte acetic anhydride in diethylene glycol monoethyl ether (DGME) serving as a low-volatility solvent, evanescent field absorption studies recording the sensor response to an increasing number of droplets deposited along the ridge surface were executed (Fig. 4). Based on the 3o-criterion, the lowest detectable volume was determined to be 18 pL (i.e., 19.4 ng of acetic anhydride). It is anticipated that further improvements on the limits of detection (LOD) could be achieved by reducing the width of the ridge waveguides such that single-mode propagation in both directions is ensured, thereby overcoming any position-dependent system response.

An even more sophisticated MIR transducer structure based on GaAs/AlGaAs was recently demonstrated with the first on-chip Mach-Zehnder interferometer (MZI) operating at MIR wavelengths.[64] Within an integrated MZI structure, photons propagate along a ridge waveguide providing single-mode behavior. The photon stream is divided by a symmetric Y-junction into two light beams equal in phase and intensity propagating along parallel waveguide arms, which are rejoined by another Y-junction into a single photon path reuniting the two beams. The addition of e.g., a sample droplet onto one of the waveguide arm leads to a change of the refractive index, and subsequently causes a delay in the phase of the propagating photons.[65,66] Therefore, a sinusoidal interference pattern is observed after recombining the phase-delayed signal carrying the analytical information with the light beam propagating along the undisturbed (i.e., reference) arm. MZI structures were microfabricated via RIE from again using 6 µm thin-film GaAs waveguiding layers deposited on top of a $Al_{0.2}Ga_{0.8}As$ optical buffer layer, which itself rests at the surface of a GaAs wafer substrate. The waveguide width of the MIR-MZI structure was selected at 5 µm following initial simulations based on finite element methods (FEM) ensuring single-mode behavior. The analytical applicability of the developed MIR-MZI was demonstrated by depositing droplets at various locations along the MZI structure resulting in different interference patterns (Fig. 5b).

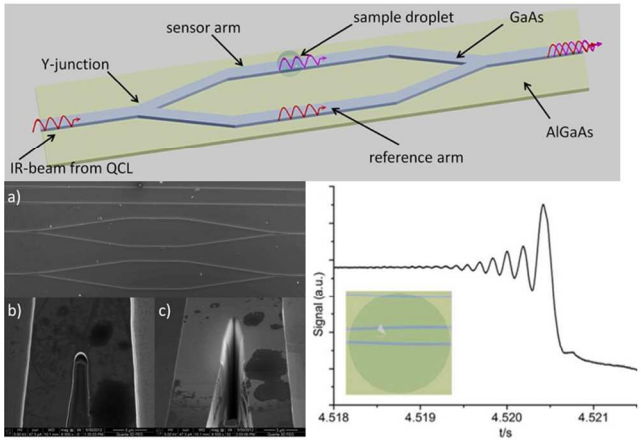

Figure 5. (top) Scheme of an on-chip MIR Mach-Zehnder interferometer. (bottom left) Scanning electron microscopy (SEM) images of MIR-MZI waveguides show (a) the top view of GaAs/AlGaAs MZIs, and the Y-junction (b) before and (c) after using focused ion beam (FIB) microscopy for refining the structure ast the joint of the waveguide arms. (bottom right) Typical interferometric signal generated by depositing e.g., water droplets at one of the MZI arms resulting in a phase delay giving rise to the observed interference pattern. Reproduced with permission from ref. [64]. Copyright 2013 American Chemical Society.

If analyte droplets – here, water - were deposited at the waveguide of the MIR-MZI leading to the first Y-junction, only an overall decrease in radiation throughput was evident resulting from the absorption of evanescently guided IR radiation. If the droplets were instead deposited onto one of the parallel Mach-Zehnder waveguide arms, a sizable interferometric response could be obtained (Fig. 5). If a water droplet was deposited directly onto the Y-junction, the interferometric signal decreased due to the linear correlation between phase shift and interaction length. Since the functionality of integrated on-chip Mach-Zehnder interferometers operating at mid-infrared wavelengths based on GaAs/AlGaAs technology has been verified, such devices may serve as highly sensitive on-chip transducer platforms for e.g., studying protein conformation changes or (bio)molecular interactions in a label-free MIR-bioassay format requiring only minute quantities of probed molecules.

Currently ongoing studies focus on the combination of MIR-MZI devices with appropriate microfluidic architectures, and on the integration of optical coupling elements based on waveguide-embedded gratings for maximizing the coupling efficiency of radiation emitted by QCLs or ICLs into the device.

Germanium Waveguides. Germanium (Ge) is a widely used material in MIR spectroscopy usually applied as a single-crystalline waveguide shaped into macroscopic ATR elements owing to its broad transparency throughout almost the entire analytically relevant MIR spectral band and beyond. Ge substrates are largely compatible to silicon processing routines,

and also provide the advantage of biocompatibility. However, the fabrication of on-chip thin-film Ge waveguides remains challenging due to considerable propagation losses observed for first-generation Ge structures. Ge waveguides on a ZnS substrate were fabricated by polishing 2 mm thick Ge prisms to a thickness of 30 µm, thereby revealing a reasonable improvement in surface sensitivity.[67]

Germanium-core fibers for optical waveguiding were fabricated by forcing a mixture of Ge and He through the central hole of a silica capillary. Afterwards, Ge was deposited at a temperature of approx. 300°C to grow into an amorphous core structure with a diameter of 5.6 and 30 µm, respectively.[68]

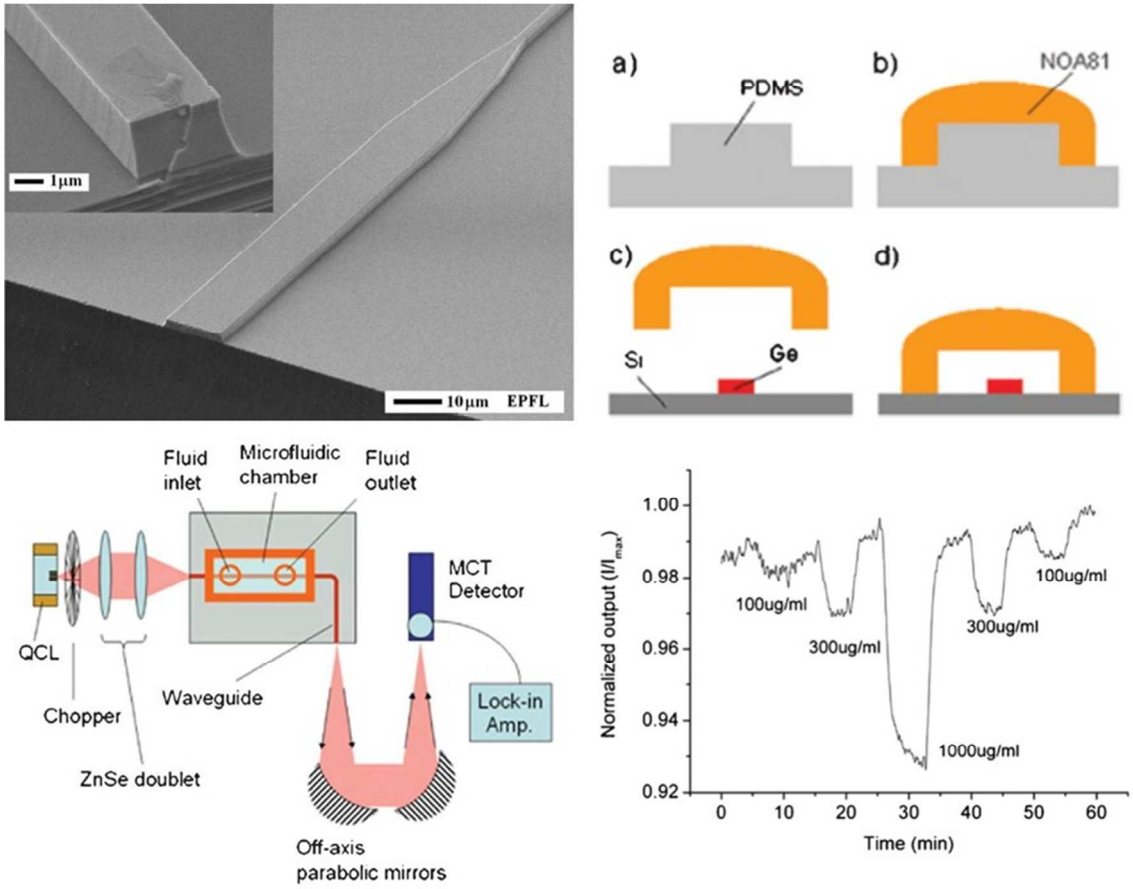

Figure 6. (top left) SEM image of a 2 µm monocrystalline germanium-on-silicon ridge waveguide. (top right) Fabrication scheme: A UV- curable adhesive (NOA81) cast onto a PDMS master, and subsequently bonded onto the silicon substrate forming a microfluidic channel, which was connected to a syringe pump. (bottom left) Optical setup: QCL radiation is coupled via lenses into the waveguide and via off-axis parabolic mirror onto a MCT detector. (bottom right) Waveguide output during a dynamic analytical study using different cocaine concentrations present at the waveguide surface determined at a wavelength of 5.8 µm. Reproduced with permission from ref. [69,70].

The group of Herzig and collaborators has pioneered the first low-loss monocrystalline on-chip Ge waveguides for applications in MIR spectroscopy using a silicon substrate. A 2 µm thin monocrystalline Ge layer was grown via reduced pressure chemical vapor deposition (RP-CVD) onto a p-type silicon substrate, which was covered by a 10 µm intrinsic silicon buffer layer in order to reduce material absorptions of the substrate.[69] The monocrystalline Ge layer provided a high optical quality, thereby facilitating low-loss Ge waveguides. Conventional photolithography was used to define waveguide structures at the Ge surface layer. Thereafter, the patterns were transferred into the wafer via RIE using CF_4, thereby obtaining high-quality single-mode waveguides. The in- and out-coupling facets of the waveguide were polished such that sufficient surface quality was provided for optical radiation coupling (Fig. 6).

The waveguides were designed at a width of 15 µm wide with a 500 µm long in-coupling segment, a 350 µm long funneling section, and a several millimeter long straight waveguide section. The latter section was designed to be single-mode at a wavelength of 5.8 µm in transverse magnetic TM polarization with a width of 2.9 µm and a thickness of 2 µm. To avoid stray light during the measurements, a 90° bend with a radius of 115 µm was inserted facilitating the analysis of samples perpendicular to the optical axis. Thereafter, a microfluidic system was integrated via rapid prototyping using NOA81, a UV-curable adhesive (Fig. 6).[70] Compared to the more commonly applied polydimethylsiloxan (PDMS), NOA81 features an improved chemical resistance, and is transparent at the required wavelength. The adhesive was cured on a PDMS or scotch-tape master, and then bonded onto the silicon substrate comprising the Ge ridge waveguide via oxygen plasma exposition. After a further curing step and a

temperature treatment at 130°C, the microfluidic assembly showed optimum adhesion. The optical setup consisted of a QCL serving as MIR radiation source at a wavelength at 5.8 µm, which was operated in continuous wave (cw) mode. IR radiation was coupled into the waveguide using a ZnSe lens doublet. After interaction of the analyte with the evanescent field within the microfluidic compartment, the emanating light was coupled onto a MCT detector via two off-axis parabolic mirrors (Fig. 6). Cocaine dissolved in tetrachloroethylene (TeCE) was selected as an exemplary analyte due to its specific absorptions at the provided QCL wavelength, and the transmission window of TeCE in this part of the MIR spectral range. Fig. 6 shows a continuous measurement of the light intensity emitted at the output facet of the Ge waveguide while the concentration of cocaine in solution was modulated. A linear relation between the cocaine concentration and the transmission drop was observed, with the smallest detected concentration at 100 µg/L. Hence, the combination of Ge waveguides and microfluidics and the potential for on-chip MIR detection of cocaine was impressively demonstrated.[71]

In particular, the integration of a microfluidic architecture suitable for MIR applications combined with single-mode waveguides facilitates the development of on-chip sample handling and – if necessary - sample preparation routines prior to the detection of analyte constituents in complex matrices.

Chalcogenide Waveguides. Chalcogenide glasses comprise a set of MIR transparent materials using different combinations of sulfur, telluride and/or selenium compounds, respectively, which are most commonly combined with arsenide, germanium, and/or gallium. In recent years, various chalcogenide glass compositions were developed such that thin-film waveguide fabrication was facilitated extending the suitable MIR spectral window up to 20 µm.[50]

Initially, chalcogenide-on-chip low loss waveguides were based on As_2Se_3/As_2S_3 grown at silicon substrates.[72] Thin-film layers of As_2S_3 serving as an optical buffer were followed by As_2Se_3 serving as the actual waveguiding core deposited via thermal evaporation onto a Si/SiO_2 substrates. As silicon has a higher refractive index compared to As_2Se_3, a cladding layer of As_2S_3 was necessary to meet optical waveguiding requirements. For lateral confinement, the photodarkening effect of As_2Se_3 was used to generate a gradual increase of the refractive index, thereby establishing single-mode buried waveguide structures. To reduce the time-consuming deposition steps, thin-film waveguides based on $Te_2As_3Se_5$ on As_2S_3 were alternatively developed.[48] Again, thermal evaporation was used to deposit $Te_2As_3Se_5$ onto commercially available As_2S_3 glass substrates with a thickness of 4 µm. Conventional optical lithography followed by physical etching in an argon atmosphere was used for defining rib waveguide structures with a width of 15 µm, and a rib height of 1.9 µm.[73] The utility of such rib structures was demonstrated coupling MIR radiation at 10.6 µm into the waveguiding structure and analyzing the propagation losses. While a variety of applications using As_2S_3 as waveguide material have been demonstrated in the visible spectral regime, MIR transmission is less common as the fabrication of rather thick waveguide films is limited due to the growth rates and the residual stress present in the deposited layers.

To overcome these limitations, a solution-casting-and-molding approach was devised for fabricating As_2S_3 waveguides in a low-cost and etch-free process. For that purpose, a PDMS mold was filled with a liquid As_2S_3 precursor via capillary forces followed by thermal treatment to obtain As_2S_3 waveguides.[74] The As_2S_3 solution was prepared by dissolving As_2S_3 in propylamine at a concentration of 0.2 g/mL, and further dilution in ethanol to reduce the viscosity of the solution. As shown in Fig. 7, a thick film of SU-8 epoxy was deposited onto a silicon substrate, and then microstructured via photolithography. Thereafter, PDMS was cast onto the pattern and cured, thus obtaining a soft mold, which defines the waveguide structure. The cured PDMS mold was placed onto a NaCl waveguide substrate, filled with the As_2S_3 precursor solution, and thermally treated to finally obtain solid waveguide structures. After an annealing step, the solution-processed As_2S_3 glass structure resembles the amorphous nature of bulk As_2S_3. Furthermore, the annealing process significantly reduced the MIR radiation losses within the waveguide structure, thereby leading to low-loss on-chip As_2S_3 waveguides feasible for MIR radiation transmission up to 9.4 µm.

This rather low-cost fabrication method for chalcogenide waveguide structures has substantial potential for providing integrated MIR chem/bio sensing structures, as the on-chip integration of QCL and waveguides is readily facilitated.[75,76]For example, a QCL structure was cleaved to obtain two facets and was mounted onto a copper substrate with a precleaved glass slide glued to the mounted QCL after establishing electrical contacts. The PDMS mold was aligned to the laser active region, filled with the As_2S_3 solution, and thermally treated to obtain a solid waveguide. After removing the precleaved substrate, a waveguide facet with sufficient optical quality was obtained. The transmittance of QCL radiation at 5 µm was detected with a MCT detector, albeit at rather high losses due to the contrast between the refractive indices of the As_2S_3 (n=2.3) and the front facet of the laser (n=3.2). Nevertheless, this strategy demonstrates at least in part the opportunity of on-chip integrated optical systems operating at MIR wavelengths.

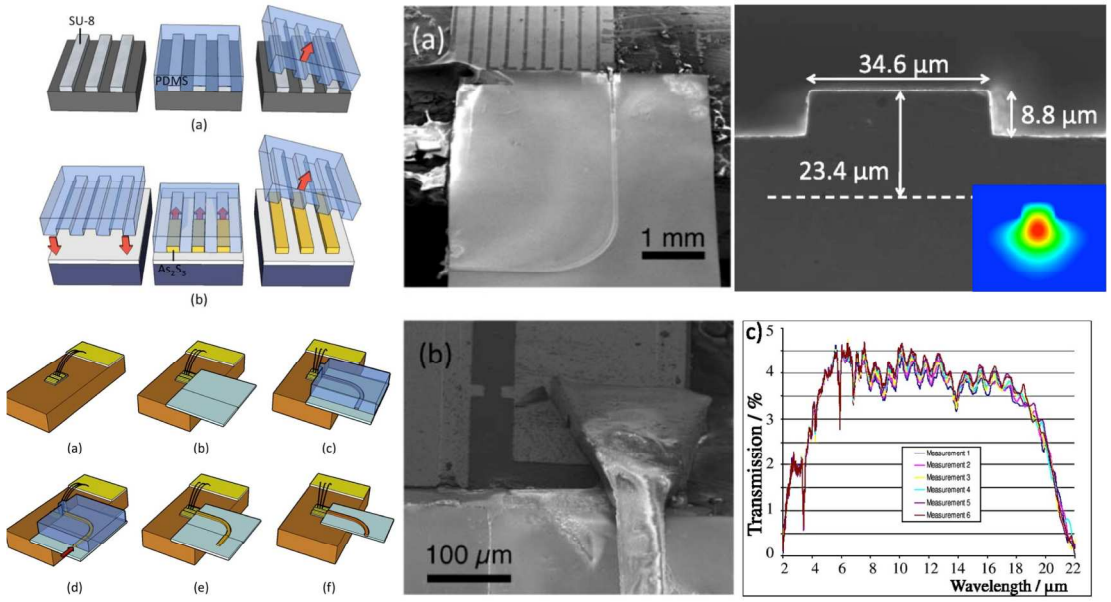

Figure 7. (left top) Fabrication scheme of As_2S_3 waveguides via solution-casting-and-molding. (left bottom) Schematic integration of chalcogenide waveguides with a QCL light source. (middle top and bottom) SEM images of integrated As_2S_3 waveguides and QCL. (right top) SEM image of a rib waveguide providing single-mode behavior at 20 µm. Single-mode profile is shown in the inset. (right bottom) Transmission spectra of a rib waveguide coupled to a Fourier transform infrared (FTIR) spectrometer and a MCT detector. Reproduced with permission from ref.[49,75,76].

However, the suitability of As_2S_3 as a cladding layer or as a waveguide, respectively, is limited due to the wavelength cut-off in the MIR regime at approx. 9.4 µm, and due to attenuation losses that are increasing with the transmitted wavelength. Hence, chalcogenide glass composites are necessary for extending the useful MIR transmission window. Therefore, compositions based on a mixture of tellurium, germanium, and gallium have been proposed as the most promising chalcogenides potentially providing MIR transparency up to 20 µm. Furthermore, these materials are suitable for thin-film fabrication, and offer tuning of the refractive index by modulating the composition of the glass.[49]

High-contrast waveguides (i.e. $\Delta n \approx 1$) were fabricated by depositing $GeTe_4$ film via RF magnetron sputtering onto a ZnSe substrate. A lift-off technique was used to obtain straight waveguides. After a waveguide pattern was photolithographically defined, a $GeTe_4$ film of about 4.6 µm in thickness was deposited onto the patterned resist. Straight waveguides were obtained once the resist was lifted off. For waveguide characterization a tunable QCL emitting at 6.4-7.5 µm was coupled into the waveguide end-facet using an As_2S_3 single-mode fiber. The transmitted light was than detected using a MIR camera.[77] For realizing single-mode waveguides operating at 20 µm, $Te_{75}Ge_{15}Ga_{10}$ (n=3.40) was selected as substrate due to its high thermal stability. A Te-Ge system was used for establishing the waveguide core, since the refractive index of Te-Ge films varies linearly with the Te-content; therefore, the refractive index can be accurately adjusted. For obtaining a refractive index divergence of approx. $4*10^{-2}$, $Te_{82}Ge_{18}$ (n=3.44) was selected as a suitable core layer composition. Thermal co-evaporation was used for depositing a $Te_{82}Ge_{18}$ thin films at 12 and 24 µm, respectively, onto the $Te_{75}Ge_{15}Ga_{10}$ substrate. Conventional photolithography followed by RIE using a mixture of CHF_3, O_2, and Ar was used to obtain rib waveguide depths of 4.5 and 9 µm ensuring single-mode waveguiding properties in the wavelength ranges of 6-11 µm and 10-20 µm, respectively.[78] Using a Fourier transform infrared spectrometer (FTIR) equipped with a liquid nitrogen cooled MCT detector, these waveguides were optical characterized. As shown in Fig. 7, the transmission window of $Te_{82}Te_{18}$ single-mode waveguides extends from 6 µm to 19 µm, which is in excellent agreement with the spectral window of telluride glasses.[49]

HgCdTe Waveguides. Mercury-cadmium-telluride (MCT) detectors are among the most commonly applied photoconductive MIR detection devices due to their high sensitivity across the entire MIR spectral band (2-24 µm). Given its utility as MIR detector material, MCT should in fact also constitute a highly attractive MIR waveguide material. Based on epitaxially grown thin-film MCT layers deposited at cadmium-telluride substrates, Mizaikoff and collaborators were able to demonstrate the first application of MCT waveguide structures serving as active transducers for MIR sensing applications. Based on such waveguides, the chip-level monolithic integration of MIR transducers/waveguides and detectors based on a single material system may be envisaged.[51] MCT thin-film waveguides were grown via MBE onto a $Cd_{0.96}Zn_{0.04}Te$ substrate (n=2.7) at a thickness of 5 µm with a determined refractive index of n=4.0. Thereafter, the MCT wafer was cleaved along the crystal axis to obtain chip dimensions of approximately 10x8 mm providing end facets with sufficient surface quality for efficient optical coupling at minimal scattering losses in the MIR regime. Afterwards, cleaved waveguide chips were aligned in an optical setup comprising a tunable QCL radiation source (5.78-6.35 µm), ZnSe lenses for accurate in- and out-coupling of the laser radiation, and a liquid-nitrogen cooled MCT detector. Droplets of diluted acetone in isopropyl alcohol were deposited at the MCT slab waveguide surface for demonstrating the analytical utility. Calibrations and measurements at 1710 cm^{-1} located at a characteristic absorption

band of acetone were executed. Damping of the radiation intensity via evanescent field absorption induced by the analyte was analyzed at different acetone concentrations providing a linear relationship. Compared to previous studies using 6 µm GaAs/AlGaAs thin-film waveguides, the performance of the 5 µm MCT thin-film waveguides appeared slightly superior.

Further sensitivity improvements are anticipated by microstructuring such MCT slab waveguides using wet/dry etching processes for obtaining improved lateral confinement, down as previously shown for GaAs thin-film structures. While no immediate benefit compared to GaAs/AlGaAs waveguides is evident, the potential of monolithically integrating waveguide and detector bears significant potential for on-chip integrated chem/bio sensing devices and lab-on-a-chip systems.

Diamond Waveguides. Besides the outstanding thermal, mechanical, and chemical characteristics of diamond, its optical properties are even more intriguing including the high refractive index, and the broad transmittance window extending into the MIR spectral regime. Diamond plays a central role in a variety of analytical applications including e.g., in electrochemistry (doped with nitrogen or boron serving as an electrode), in atomic force microscopy (ultra-hard scanning probe tips), and in IR-ATR spectroscopy (robust ATR elements, mostly hemispheres). Advantageously, diamond is characterized by a small thermal expansion coefficient, extreme hardness, and inertness to most chemicals. Furthermore, given the flexibility in surface termination, diamond surfaces may be tailored to accommodating a wide range of attachment and immobilization chemistries for establishing sophisticated chem/bio sensing architectures. Hence, diamond inherently lends itself as an interesting candidate material for on-chip MIR waveguides enabling advanced chem/bio sensing structures. However, until recently structuring of diamond as MIR waveguides was limited to RIE processes, which provide only limited control on the sidewall roughness requiring subsequent focused ion beam (FIB) processing steps for obtaining suitably smooth waveguide facets at the required optical quality.

The group of Karlsson and collaborators has introduced an inductively coupled plasma (ICP) etching process leading to a sidewall roughness of sufficient optical quality facilitating the application of diamond structures as free-standing thin-film waveguides.[79,80] In collaboration with the Mizaikoff team, polycrystalline diamond films with a thickness of 13-15 µm were grown via microwave plasma assisted chemical vapor deposition (MW-CVD) onto a 200 nm layer of Si_3N_4 and 2 µm of SiO_2 at a Si wafer substrate. As the refractive index of diamond (n=2.38) is lower than the refractive index of silicon (n=3.5) at MIR wavelengths, cladding layers of Si_3N_4 (n=2.0) and SiO_2 (n=1.46) are necessary to fulfill the optical waveguiding requirements in this spectral regime.

To define diamond strip waveguide structures, conventional photolithography in combination with ICP etching was applied. For this purpose, a 1.7 µm Al layer was sputtered onto the diamond layer, structured via photolithography, and the pattern transferred into the Al layer via ICP based on chlorine chemistry (i.e., BCl_3/Cl_2). The diamond layer was subsequently etched via ICP using $O_2/Ar/SF_6$, and the Al layer serving as etching mask was removed using acids. Thereafter, RIE followed by hydrofluoric acid (HF) etching was applied for obtaining free-standing thin-film diamond strip waveguides. These waveguide structures were aligned in an optical setup comprising a tunable QCL (5.78 -6.35 µm), a 3D-translation stage, and a liquid nitrogen cooled MCT detector. Following a calibration procedure, the lowest detectable analyte volume was determined at 18 pL, which - prior to any optimization of the waveguide width (i.e., additional lateral confinement) – readily compares to already optimized GaAs strip waveguides in terms of sensitivity.[40] Further optimization of these waveguide structures is envisaged by decreasing the thickness of the diamond core layer, and via additional lateral confinement strategies. Combined with a tunable QCL, the detection of anisaldehyde as a model analyte was demonstrated for these first thin-film diamond waveguide prototypes.

Silicon-Based Waveguides Materials. Silicon-on-insulator (SOI) and silica-on-silicon are the most prevalent material platforms for waveguide-based sensors operating at visible and NIR wavelengths.[81] These platforms readily take advantage of complementary metal-oxide-semiconductor (CMOS) fabrication and processing techniques. The feasibility of silicon-on-insulator (SOI)[82–85] and silicon-on-sapphire (SOS)[63,86,87] as a waveguide platform has been recently demonstrated for wavelengths up to 5.6 µm. While monocrystalline Si provides optical transparency up to 8 µm, the accessible spectral windows of silicon dioxide and sapphire are limited to approx. 3.7 and 6 µm, respectively. Pedestal air-clad silicon[88,89] and crystalline Si on porous silicon[82,90] waveguide systems were realized to overcome the wavelength limitations arising from the opacity of SiO_2 and sapphire. However, complex fabrication strategies including multiple thin-film growth and selective etching steps has limited device development and more widespread application.

An alternative approach are silicon-on-nitride waveguides, whereby silicon nitride (SiN) serves as an optical buffer layer and Si as both, the actual waveguide and the substrate. SiN has a wide optical transparency window from the visible regime up to 8.5 µm in the MIR.[91] Silicon-on-insulator (SOI) dies were coated with a 1.3 µm SiN layer via plasma-enhance chemical vapor deposition (PECVD), and a 50 nm thick SiO_2 adhesion layer. Thereafter, a silicon die - also coated with a 50 nm adhesion layer - was bonded onto SiN using spin-on glass (SOG) as a bonding agent. After lapping and wet etching in tetramethylammonium hydroxid (TMAH), the buried oxide layer of the initial SOI structure was removed using hydrofluoric acid, thereby exposing silicon thin-film waveguide structures. Rib waveguides were obtained via inductively coupled-plasma (ICP) etching using a SiO_2 hard mask providing single mode behavior at a wavelength at 3.39 µm for a rib thickness of 2 µm, 0.8 µm rib-etching depth, and a rib width of 2.5 µm.[92]

SiN can be fully integrated into CMOS processes, and provides a high chemical stability and mechanical robustness rendering SiN a suitable material for chem/bio sensors. SiN thin-film waveguides can be grown via low-pressure vapor deposition (LPCVD) on top of SiO_2 coated Si wafers, and structured via photolithography and ICP-RIE. The utility of SiN waveguides was demonstrated at 3.75 µm for 2.5 µm thick and 4 µm wide single-mode ridge waveguides on top of a 4 µm SiO_2 optical buffer layer.[42,93]

Besides silicon-based materials, germanium tin alloys (GeSn)[45], silicon germanium tin alloys (SiGeSn)[94], and aluminum nitride (AlN)[44] were proposed as a thin-film waveguide material for extending the spectral window up to 15 µm while benefitting from standard CMOS processing techniques. AlN thin-film waveguides were successfully introduced for the wavelength window 2.4-2.7µm by sputtering thin films of AlN onto a thermally grown SiO_2 layer. Electron-beam lithography and subsequent reactive ion etching resulted in single mode waveguides with a width of 10 µm and a height of 1 µm.[44]

TOWARDS ON-CHIP CHEM/BIO SENSORS AND IR-LAB-ON-A-CHIP

While MIR based optical chemical sensors nowadays already more commonly used, only few biosensors based on mid-infrared technologies are reported. This is mainly attributable to the insufficient sensitivity provided by currently proposed MIR sensing platforms, and which is particularly relevant for detecting minute quantities of biomolecules such as proteins, DNA, etc. The principal feasibility of label-free DNA detection via hybridization using surface-modified MIR waveguides was recently shown.[95] After immobilization of ssDNA at the surface of a ZnSe ATR-crystal, binding of a complementary strand was monitored via conventional FTIR spectroscopy. However, such label-free MIR biosensing approaches are frequently still limited in sensitivity, and require complex molecular surface architectures, and suffer from spectral interferences by the immobilization and background matrices (e.g. water, blood, urine, etc.).

Hence, strategies for significantly enhancing the sensitivity without additional recognition or enrichment schemes, simplified surface modification procedures, reduction of the required sample amount, volume and/or concentration, and reduction of matrix interferences are essential for establishing competitive MIR biosensors and bioassay technologies.

Next to waveguide-based enhancements discussed in this feature, additional concepts may aid in increasing the sensitivity of MIR chem/bio sensing devices, e.g., via the introduction of surface enhanced infrared absorption (SEIRA) strategies. Albeit not as pronounced as observed in surface enhanced raman spectroscopy (SERS), metallic nanostructures and nanoparticles (i.e., Au, Ag, Pt, etc.) are known to significantly enhance infrared absorption signatures as well. The feasibility of combining SEIRA effects with thin-film waveguide materials was recently demonstrated for As_2S_3 glass waveguides using gold nanoparticles for increasing the strength of MIR absorption features for 4-Nitrothiophenol deposited at the surface of thus modified substrates.[96] Likewise, enhancement factors of up to 300,000 were reported using sophisticated deposition strategies resulting in 1.5 µm long gold nanowires (i.e. 100 nm in diameter) on a CaF_2 substrate.[97]

Next to these optical/physical enhancement strategies, chemical enhancement via – more or less molecularly selective - enrichment of the constituents of interest at or near to the waveguide surface (i.e., within the evanescent field) has shown significant potential. Advantageously, enrichment schemes in MIR sensing do not necessarily need to provide exclusive selectivity, as the inherent molecular specification via IR fingerprint absorptions may efficiently combine with chem/bio recognition and/or enrichment approaches. However, using additional (bio)molecular immobilization architectures at the waveguide surface frequently also leads to additional spectral interferences, which requires diligent design of such recognition elements.

For less complex analyte molecules, rather simple surface modification approaches using e.g., conventional aliphatic polymers serving as physic-chemical enrichment membrane via largely polarity-based reversible partitioning effects facilitate label-free analysis of low-concentrated analytes e.g., in aqueous solution. Exemplarily, volatile and semi-volatile organic constituents (VOCs and SVOCs) have been determined at µg/L (i.e., low ppb) levels in various aqueous matrices including surface waters, aquifers, and even sea water.[98–104]

With the integration of suitable microfluidic structures on top of a waveguide, sophisticated extraction and enrichment strategies may be introduced, as recently shown for the detection of cocaine in human salvia.[71] Thereby, the analysis of real-world biomedical samples such as e.g., blood, plasma, saliva or urine providing on-chip or on-device sample preparation clearly benefits more complex IR-lab-on-a-chip (LOC) approaches.

CONCLUSIONS

In conclusion, by expanding the range of available MIR transparent waveguides using alternative materials such as semiconductors, diamond, etc. readily serving as thin-film waveguides, the 'optical gap' between advanced MIR light sources and detectors may be closed facilitating full – monolithic or hybrid - integration of mid-infrared sensing devices, and more generically, versatile MIR chem/bio sensing and assay platforms. Next to evident progress in MIR light source and detector technology, the diversity of applicable thin-film waveguide materials and their physical, optical, and chemical properties facilitate translating conventional fiberoptic sensing technologies in the 3-15 µm spectral band into sophisticated on-chip photonic structures and devices taking advantage of ring resonators, disc resonators, slot waveguides, solid-state interferometers, etc. Evidently, only the combination of inherent molecular selectivity and high analytical sensitivity may lead to next-generation label-free chem/bio sensors and assays; hence, it is safe to conclude that given the current technological advancements, mid-infrared technologies will evolve into a competitive analytical toolbox serving to these needs.

AUTHOR INFORMATION

Corresponding Author

*E-mail: boris.mizaikoff@uni-ulm.de.

The authors declare no competing financial interest.

Prof. Boris Mizaikoff joined the faculty at Ulm University, Germany as a Chaired Professor and Director at the Institute of Analytical and Bioanalytical Chemistry (IABC) in 2007 with prior appointments at the Vienna University of Technology (Austria), and at the Georgia Institute of Technology (Atlanta/GA, USA). His research interests focus on optical chem/bio sensors, tailored (bio)molecular recognition interfaces, molecularly imprinted materials, system miniaturization and integration, and multifunctional (nano)analytical tech-

niques with applications in environmental analysis, process monitoring, and biomedical diagnostics.

Markus Sieger is a Ph.D. student at IABC working on mid-infrared waveguide technologies and their application in chem/bio sensor systems.

ACKNOWLEDGMENTS

This study has in part been supported by the European Union's Seventh Framework Programme managed by REA Research Executive Agency http://ec.europa.eu/rea (FP7/2007-2013) under grant agreement no. 314018 FP7-SME-2012-SME (MYCOSPEC). Furthermore, the authors gratefully acknowledge partial support by the Kompetenznetz Funktionelle Nanostrukturen Baden Wuerttemberg, Germany.

REFERENCES

(1) Mizaikoff, B. *Anal. Chem.* **2003**, *75*, 258 A – 267 A.

(2) Rotermund, F.; Petrov, V.; Noack, F. *Opt. Commun.* **2000**, *185*, 177–183.

(3) Kim, S.-S.; Young, C.; Mizaikoff, B. *Anal. Bioanal. Chem.* **2008**, *390*, 231–237.

(4) Lin, C. H.; Yang, R. Q.; Zhang, D.; Murry, S. J.; Pei, S. S.; Allerman, A. A.; Kutz, S. R. *Electron. Lett.* **1997**, *33*, 598–599.

(5) Faist, J.; Capasso, F.; Sivco, D. L.; Sirtori, C.; Hutchinson, A. L.; Cho, A. Y. *Science* **1994**, *264*, 553–556.

(6) Kazarinov, R. F.; Suris, R. A. *Sov. Physics-Semiconductors* **1971**, *5*, 707–709.

(7) Yang, R. Q. *Superlattices Microstruct.* **1995**, *17*, 77–83.

(8) Saleh, B. E. A.; Teich, M. C. *Fundamentals of Photonics*, 2nd ed.; Saleh, B. E. A., Teich, M. C., Eds.; John Wiley & Sons Ltd.: New Jersey, 2007.

(9) Capasso, F.; Sivco, D.; Gmachl, C.; Cho, A. Y. *Phys. Today* **2002**, *55*, 34–40.

(10) Charlton, C.; Giovannini, M.; Faist, J.; Mizaikoff, B. *Anal. Chem.* **2006**, *78*, 4224–4227.

(11) Young, C.; Kim, S.-S.; Luzinova, Y.; Weida, M.; Arnone, D.; Takeuchi, E.; Day, T.; Mizaikoff, B. *Sensors Actuators B Chem.* **2009**, *140*, 24–28.

(12) Charlton, C.; Katzir, A.; Mizaikoff, B. *Anal. Chem.* **2005**, *77*, 4398–4403.

(13) Gendron, L.; Koeniguer, C.; Berger, V.; Marcadet, X. *Appl. Phys. Lett.* **2005**, *86*, 121116.

(14) Bauer, S.; Lang, S. B. *Dielectr. Electr. Insul. IEEE Trans.* **1996**, *3*, 647–676.

(15) Muralt, P. *Reports Prog. Phys.* **2001**, *64*, 1339–1388.

(16) Schettino, E. *Ann. Sci.* **1989**, *46*, 511–517.

(17) Alexander Graf Gerald Gerlach, Mi. A. *Proc. Est. Acad. Sci. Eng* **2007**, *13*, 338–353.

(18) Rogalski, A. *Reports Prog. Phys.* **2005**, *68*, 2267–2336.

(19) Karlowatz, M.; Kraft, M.; Mizaikoff, B. *Anal. Chem.* **2004**, *76*, 2643–2648.

(20) Janotta, M.; Vogt, F.; Voraberger, H.-S.; Waldhauser, W.; Lackner, J. M.; Stotter, C.; Beutl, M.; Mizaikoff, B. *Anal. Chem.* **2004**, *76*, 384–391.

(21) Zhang, X. H.; Ma, H. L.; Fonteneau, G.; Lucas, J. *J. Non. Cryst. Solids* **1992**, *140*, 47–51.

(22) Le Neindre, L.; Smektala, F.; Le Foulgoc, K.; Zhang, X. .; Lucas, J. *J. Non. Cryst. Solids* **1998**, *242*, 99–103.

(23) MacDonald, S.; Michel, K.; LeCoq, D.; Boussard-Pledel, C.; Bureau, B. *Opt Mater* **2004**, *25*, 171.

(24) Harrick, N. J. *Internal Reflection Spectroscopy*; Harrick, N. J., Ed.; Wiley: New York, 1967.

(25) Axelrod, D.; Burghardt, T. P.; Thompson, N. L. *Annu. Rev. Biophys. Bioeng.* **1984**, *13*, 247–268.

(26) Wang, R. P. *Amorphous Chalcogenides: Advances and Applications*; Pan Stanford Publishing Pte Ltd: Singapore, 2014.

(27) Bradshaw, J. T.; Mendes, S. B.; Saavedra, S. S. *Anal. Chem.* **2005**, 29A – 36A.

(28) Mendes, S. B.; Saavedra, S. S. *Appl. Opt.* **2000**, *39*, 612–621.

(29) Tamir, T.; Garmire, E.; Hammer, J. H.; Kogelnik, H.; Zernike, F. *Topics in Applied Physics: Integrated Optics*, 2nd ed.; Kogelnik, H., Ed.; Springer-Verlag: Berlin, 1979.

(30) Wang, X.; Kim, S.-S.; Roßbach, R.; Jetter, M.; Michler, P.; Mizaikoff, B. *Analyst* **2012**, *137*, 2322.

(31) Doerr, C. R.; Kogelnik, H. *J. Light. Technol.* **2008**, *26*, 1176–1187.

(32) Harrington, J. A. In *SPIE Press*; 2004.

(33) Sanghera, J.; Aggarwal, I. In *CRC Press*; 1998.

(34) Katzir, A. *Lasers and Optical Fibers in Medicine*; Academic Press Limited: London, 1993.

(35) Kozma, P.; Kehl, F.; Ehrentreich-Förster, E.;

Stamm, C.; Bier, F. F. *Biosens. Bioelectron.* **2014**, *58*, 287–307.

(36) Okamot, K. *Fundamentals of Optical Waveguides*, 2nd ed.; Academic Press Limited, 2005.

(37) Snyder, A. W.; Love, J. *Optical Waveguide Theory*; Springer, Ed.; New York, 1984.

(38) Edwards, D. F.; Ochoa, E. *Appl. Opt.* **1980**, *19*, 4130–4131.

(39) Palik, E. D. *Handbook of Optical Constants of Solids*; Bertrams, 1997.

(40) Wang, X.; Karlsson, M.; Forsberg, P.; Sieger, M.; Nikolajeff, F.; Osterlund, L.; Mizaikoff, B. *Anal. Chem.* **2014**, *86*, 8136–8141.

(41) Brückner, R. *J. Non. Cryst. Solids* **1971**, *5*, 177–216.

(42) Lin, P. T.; Singh, V.; Lin, H.-Y. G.; Tiwald, T.; Kimerling, L. C.; Agarwal, A. M. *Adv. Opt. Mater.* **2013**, *1*, 732–739.

(43) Kischkat, J.; Peters, S.; Gruska, B.; Semtsiv, M.; Chashnikova, M.; Klinkmüller, M.; Fedosenko, O.; Machulik, S.; Aleksandrova, A.; Monastyrskyi, G.; Flores, Y.; Ted Masselink, W. *Appl. Opt.* **2012**, *51*, 6789–6798.

(44) Lin, P. T.; Jung, H.; Kimerling, L. C.; Agarwal, A.; Tang, H. X. *Laser Photon. Rev.* **2014**, *8*, L23–L28.

(45) Soref, R. a; Emelett, S. J.; Buchwald, W. R. *J. Opt. A Pure Appl. Opt.* **2006**, *8*, 840–848.

(46) Icenogle, H. W.; Platt, B. C.; Wolfe, W. L. *Appl. Opt.* **1976**, *15*, 2348–2351.

(47) Bass, M.; DeCusatis, C.; Enoch, J.; Lakshminarayanan, V.; Li, G.; MacDonald, C.; Mahajan, V.; Van Stryland, E. *Handbook of Optics*; McGraw-Hill Professional: New York, 2009.

(48) Vigreux-Bercovici, C.; Bonhomme, E.; Pradel, A.; Broquin, J.-E.; Labadie, L.; Kern, P. *Appl. Phys. Lett.* **2007**, *90*, 011110.

(49) Vigreux, C.; Barthélémy, E.; Bastard, L.; Broquin, J.; Barillot, M.; Ménard, S.; Parent, G.; Pradel, A. *Opt. Lett.* **2011**, *36*, 2922–2924.

(50) Danto, S.; Houizot, P.; Boussard-Pledel, C.; Zhang, X.-H.; Smektala, F.; Lucas, J. *Adv. Funct. Mater.* **2006**, *16*, 1847–1852.

(51) Wang, X.; Antoszewski, J.; Putrino, G.; Lei, W.; Faraone, L. 1–6.

(52) Djuric, Z.; Jaksic, Z.; Djinovic, Z.; Jovic, V. *Mater. Sci. Forum* **1998**, *282-283*, 131–138.

(53) Spott, A.; Liu, Y.; Baehr-Jones, T.; Ilic, R.; Hochberg, M. *Appl. Phys. Lett.* **2010**, *97*, 213501.

(54) Nedeljkovic, M.; Khokhar, a. Z.; Hu, Y.; Chen, X.; Penades, J. S.; Stankovic, S.; Chong, H. M. H.; Thomson, D. J.; Gardes, F. Y.; Reed, G. T.; Mashanovich, G. Z. *Opt. Mater. Express* **2013**, *3*, 1205–1214.

(55) Lin, P. T.; Kwok, S. W.; Lin, H.-Y. G.; Singh, V.; Kimerling, L. C.; Whitesides, G. M.; Agarwal, A. *Nano Lett.* **2014**, *14*, 231–238.

(56) Chen, Y.; Lin, H.; Hu, J.; Li, M. *ACS Nano* **2014**, *8*, 6955–6961.

(57) Chiles, J.; Fathpour, S. *Optica* **2014**, *1*, 350–355.

(58) Dang, Z.; Banas, A.; Azimi, S.; Song, J.; Breese, M.; Yao, Y.; Turaga, S. P.; Recio-Sánchez, G.; Bettiol, A.; Kan, J. Van. *Appl. Phys. A* **2013**, *112*, 517–523.

(59) Duan, C.; Wang, W.; Xie, Q. *Biomicrofluidics* **2013**, *7*, 026501.

(60) Eijkel, J. C. T.; Berg, A. van den. *Microfluid. Nanofluidics* **2005**, *1*, 249–267.

(61) Lin, H.; Li, L.; Deng, F.; Ni, C.; Danto, S.; Musgraves, J. D.; Richardson, K.; Hu, J. *Opt. Lett.* **2013**, *38*, 2779–2782.

(62) Shankar, R.; Leijssen, R.; Bulu, I.; Lončar, M. *Opt. Express* **2011**, *19*, 5579–5586.

(63) Shankar, R.; Bulu, I.; Lončar, M. *IEEE Int. Conf. Gr. IV Photonics GFP* **2013**, *051108*, 17–18.

(64) Sieger, M.; Balluff, F.; Wang, X.; Kim, S.; Leidner, L.; Gauglitz, G.; Mizaikoff, B. *Anal. Chem.* **2013**, *85*, 3050–3052.

(65) Prieto, F.; Sepulveda, B.; Calle, A.; Llobera, A.; Dominguez, C.; Abad, A.; Montoya, A.; Lechuga, L. M. *Nanotechnology* **2003**, *907*, 907–912.

(66) Ingenhoff, J.; Drapp, B.; Gauglitz, G. *Fresenius J. Anal. Chem.* **1993**, *346*, 580–583.

(67) Plunkett, S. E.; Propst, S.; Braiman, M. S. *Appl. Opt.* **1997**, *36*, 4055–4061.

(68) Mehta, P.; Krishnamurthi, M.; Healy, N.; Baril, N. F.; Sparks, J. R.; Sazio, P. J. a.; Gopalan, V.; Badding, J. V.; Peacock, A. C. *Appl. Phys. Lett.* **2010**, *97*, 071117.

(69) Chang, Y.-C.; Paeder, V.; Hvozdara, L.; Hartmann, J.-M.; Herzig, H. P. *Opt. Lett.* **2012**, *37*, 2883–2885.

(70) Chang, Y.-C.; Wägli, P.; Paeder, V.; Homsy, A.; Hvozdara, L.; van der Wal, P.; Di Francesco, J.; de

Rooij, N. F.; Peter Herzig, H. *Lab Chip* **2012**, *12*, 3020–3023.

(71) Wägli, P.; Chang, Y. C.; Homsy, A.; Hvozdara, L.; Herzig, H. P.; De Rooij, N. F. *Anal. Chem.* **2013**, *85*, 7558–7565.

(72) Hô, N.; Phillips, M. C.; Qiao, H.; Allen, P. J.; Krishnaswami, K.; Riley, B. J.; Myers, T. L.; Anheier, N. C. *Opt. Lett.* **2006**, *31*, 1860–1862.

(73) Vigreux-Bercovici, C.; Ranieri, V.; Labadie, L.; Broquin, J.-E.; Kern, P.; Pradel, a. *J. Non. Cryst. Solids* **2006**, *352*, 2416–2419.

(74) Tsay, C.; Mujagić, E.; Madsen, C. K.; Gmachl, C. F.; Arnold, C. B. *Opt. Express* **2010**, *18*, 15523–15530.

(75) Tsay, C.; Toor, F.; Gmachl, C. F.; Arnold, C. B. *Opt. Lett.* **2010**, *35*, 3324–3326.

(76) Tsay, C.; Zha, Y.; Arnold, C. B. *Opt. Express* **2010**, *18*, 26744–26753.

(77) Mittal, V.; Aghajani, A.; Carpenter, L. G.; Gates, J. C.; Butement, J.; Smith, P. G. R.; Wilkinson, J. S.; Murugan, G. S. *Opt. Lett.* **2015**, *40*, 2016–2019.

(78) Vigreux, C.; Sousa, S. De; Foucan, V.; Barthélémy, E.; Pradel, A. *Microelectron. Eng.* **2011**, *88*, 222–227.

(79) Forsberg, P.; Karlsson, M. *Opt. Express* **2013**, *21*, 2693–2700.

(80) Karlsson, M.; Nikolajeff, F. *Opt. Express* **2003**, *11*, 502–507.

(81) Yamada, K. *Silicon Photonics II*; Lockwood, D. J., Pavesi, L., Eds.; Topics in Applied Physics; Springer Berlin Heidelberg: Berlin, Heidelberg, 2011; Vol. 119.

(82) Muneeb, M.; Chen, X.; Verheyen, P.; Lepage, G.; Pathak, S.; Ryckeboer, E.; Malik, a; Kuyken, B.; Nedeljkovic, M.; Van Campenhout, J.; Mashanovich, G. Z.; Roelkens, G. *Opt. Express* **2013**, *21*, 11659–11669.

(83) Liu, X.; Kuyken, B.; Roelkens, G.; Baets, R.; Osgood, R. M.; Green, W. M. J. *Nat. Photonics* **2012**, *6*, 667–671.

(84) Zlatanovic, S.; Park, J. S.; Moro, S.; Boggio, J. M. C.; Divliansky, I. B.; Alic, N.; Mookherjea, S.; Radic, S. *Nat. Photonics* **2010**, *4*, 561–564.

(85) Kuyken, B.; Liu, X.; Osgood Jr., R. M.; Baets, R.; Roelkens, G.; Green, W. M. J. *Opt. Express* **2011**, *19*, 20172.

(86) Li, F.; Jackson, S. D.; Grillet, C.; Magi, E.; Hudson, D.; Madden, S. J.; Moghe, Y.; O'Brien, C.; Read, A.; Duvall, S. G.; Atanackovic, P.; Eggleton, B. J.; Moss, D. J. *Opt. Express* **2011**, *19*, 15212.

(87) Baehr-Jones, T.; Spott, A.; Ilic, R.; Spott, A.; Penkov, B.; Asher, W.; Hochberg, M. *Opt. Express* **2010**, *18*, 12127–12135.

(88) Lin, P. T.; Singh, V.; Hu, J.; Richardson, K.; Musgraves, J. D.; Luzinov, I.; Hensley, J.; Kimerling, L. C.; Agarwal, A. *Lab Chip* **2013**, *13*, 2161–2166.

(89) Lin, P. T.; Singh, V.; Cai, Y.; Kimerling, L. C.; Agarwal, A. *Opt. Lett.* **2013**, *38*, 1031–1033.

(90) Mashanovich, G. Z.; Milošević, M. M.; Nedeljkovic, M.; Owens, N.; Xiong, B.; Teo, E. J.; Hu, Y. *Opt. Express* **2011**, *19*, 7112–7119.

(91) Mu, J.; Soref, R.; Kimerling, L. C.; Michel, J. *Appl. Phys. Lett.* **2014**, *104*, 2012–2016.

(92) Khan, S.; Chiles, J.; Ma, J.; Fathpour, S. *Appl. Phys. Lett.* **2013**, *102*, 121104.

(93) Lin, P. T.; Singh, V.; Kimerling, L.; Agarwal, A. M. *IEEE SENSORS 2013 - Proc.* **2013**, No. Shipley 1813, 1–4.

(94) Soref, R. *Nat. Photonics* **2010**, *4*, 495–497.

(95) Riccardi, C. S.; Hess, D. W.; Mizaikoff, B. *Analyst* **2011**, *136*, 4906–4911.

(96) Verger, F.; Pain, T.; Nazabal, V.; Boussard-Plédel, C.; Bureau, B.; Colas, F.; Rinnert, E.; Boukerma, K.; Compère, C.; Guilloux-Viry, M.; Deputier, S.; Perrin, a.; Guin, J. P. *Sensors Actuators B Chem.* **2012**, *175*, 142–148.

(97) Neubrech, F.; Pucci, A.; Cornelius, T. W.; Karim, S.; García-Etxarri, A.; Aizpurua, J. *Phys. Rev. Lett.* **2008**, *101*, 157403.

(98) Lu, R.; Sheng, G.; Li, W.; Yu, H.; Raichlin, Y.; Katzir, A.; Mizaikoff, B. *Angew. Chemie - Int. Ed.* **2013**, *52*, 2265–2268.

(99) Regan, F.; Walsh, F.; Walsh, J. *Int. J. Environ. Anal. Chem.* **2003**, *83*, 621–631.

(100) Pejcic, B.; Myers, M.; Ross, A. *Sensors* **2009**, *9*, 6232–6253.

(101) Schaedle, T.; Pejcic, B.; Myers, M.; Mizaikoff, B. *Anal. Chem.* **2014**, *86*, 9512–9517.

(102) Gonzalvez, A.; Garrigues, S.; de la Guardia, M.; Armenta, S. *Anal. Methods* **2011**, *3*, 43–52.

(103) Flavin, K.; Hughes, H.; Dobbyn, V.; Kirwan, P.; Murphy, K.; Steiner, H.; Mizaikoff, B.; Mcloughlin, P. *Int. J. Environ. Anal. Chem.* **2006**,

86, 401–415.

(104) Murphy, B.; Mcloughlin, P. *Int. J. Environ. Anal. Chem.* **2003**, *83*, 653–662.

TOC

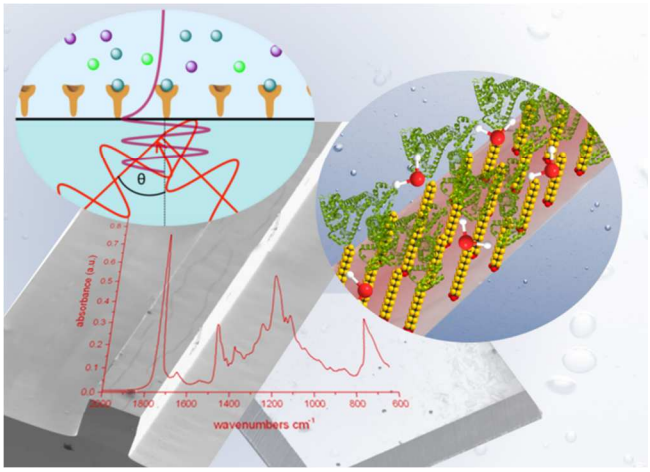

Insert Table of Contents artwork here